Electromagnetic Analysis for Interior Permanent-Magnet Machine Using Hybrid Subdomain Model

Zhaokai Li ⓘ, Xiaoyan Huang ⓘ, *Member, IEEE*, Zhuo Chen ⓘ, Lijian Wu ⓘ, *Senior Member, IEEE*, Yiming Shen ⓘ, and Tingna Shi ⓘ, *Member, IEEE*

Abstract—This paper proposed a hybrid subdomain model (HSM) for calculating the magnetic field distribution of interior permanent-magnet (IPM) machine accounting for slotting effect, rotor saliency, and iron nonlinearity. In the constant permeability region, i.e., slots, slot-opening, and air-gap, three subdomains are introduced to represent their magnetic field. By applying the subdomains interface conditions and nonlinear boundary conditions, the analytical air-gap field solution can be obtained based on the governing Laplace and Poisson equation. For the iron region, the magnetic reluctance network (MRN) is proposed to account for rotor saliency iron and nonlinearity. The magnetic voltage source is introduced to represent the permanent-magnet (PM) while the air-gap flux source is used to replace the air-gap reluctance network, which is the key to guarantee the computational efficiency and high accuracy. The electromagnetic performances of both flat-shaped and V-shaped IPM machines are investigated to show the advantages of different IPM machine topologies analytically. The HSM predictions for both IPM machines are validated by finite-element (FE) analysis and experimental results.

Index Terms—Subdomain model, magnetic reluctance network, slotting effect, rotor saliency, iron nonlinearity.

I. INTRODUCTION

THE demand of IPM machines has been greatly increased in electric-vehicle, aerospace, and industrial application due to high torque density, high efficiency, and great flux-weakening capability [1]–[3]. To accurately predict the performance of IPM machines, finite-element method (FEM) is always employed and many commercial FE software, e.g., Ansys, JMAG, and FLUX, are developed to satisfy the demand [4]–[6]. Although FE analysis is powerful for modelling the complex geometry of electric machines with high accuracy, the computational burden is too heavy, especially for parametric design and optimization at initial stage. Hence, many magnetic-circuit-based models and analytical models are proposed to reduce the calculation time.

In the magnetic-circuit-based model, both lumped parameter magnetic circuit (LPMC) and magnetic reluctance network (MRN) have been widely researched as they can account for the iron nonlinearity. The main concept of LPMC and MRN is to transform the abstract field distribution into visible magnetic circuit, which is similar to electric circuit. For the LPMC, the IPM machine was divided into the magnetic reluctances of stator yoke, stator tooth, air-gap, rotor bridge, rotor yoke, and PM, where the flux density in each part is obtained based on the flux tube theory and Kirchhoff's voltage law [7]–[13]. Hence, the rough values of magnetic field in these regions are obtained. As for MRN, the magnetic reluctance is established based on the certain mesh approaches. Liu *et al*. proposed quadrilateral segmentation approach and hexagonal segmentation approach to analyze PM vernier machine using MRN [14], [15]. The equivalent permeability with different shapes was also investigated to form a new MRN [16]. New air-gap model was proposed to show the machine motion in [17]. The reluctance number was optimized to improve the calculation efficiency and keep the high accuracy [18]. Although the MRN of IPM machine is easy to establish, it is required to form new MRN at different rotor position due to the change of air-gap flux. Adjusting the air-gap reluctance in MRN is complicated and inevitably leads to numerical errors. Besides, there are considerable air reluctances in MRN to achieve high calculation accuracy. Since the calculation time of MRN largely depends on the reluctance number, it is difficult to improve the calculation efficiency.

The 1-D analytical model can be incorporated into the magnetic circuit or network model to improve the accuracy. Winding function theory combined with LPMC was proposed to predict the air-gap field of IPM machines [19]–[21]. The equivalent air-gap function was improved to compute the armature reaction field considering the variation of air-gap permeance to the rotor position [22], [23]. These models based on 1-D analytical model have high computational efficiency but show low accuracy in predicting slotted air-gap [19]–[23].

2-D analytical models have been widely used for surface-mounted PM (SPM) machines as they have large effective air-gap. However, these models always assume infinite permeability for iron region [24]–[28], which leads to large errors. Hence, the LPMC was used to assist with the conformal mapping

model [29]–[30] or subdomain model [31], [32] to improve the prediction accuracy for SPM machines. However, these models neglect the nonlinear permeability of rotor, which will lead to large errors for IPM machines.

As the rotor nonlinearity and saliency play an important role in the performance of IPM machines, it is complicated and difficult to directly develop the 2-D analytical model for IPM machines. The open-circuit performance of IPM machines has been investigated using conformal mapping or subdomain due to its simple flux distribution [33]–[38]. As for on-load performance, the conformal mapping combined with MRN is introduced to investigate the IPM machines considering both saturation effect and saliency effect [39]. However, it requires much numerical computation for the transformation of equivalent current position between the slotless and slotted domains. The subdomain model of spoke-type IPM machine has been derived under on-load condition [40]–[45], but the infinitely permeable iron was still assumed and therefore the rotor saliency cannot be considered in [40]–[44]. In [45], the FEM result was required to consider the saturation of rotor, which neglects the influence of armature reaction on the rotor saturation. According to published literature, there are few works on the subdomain model for the on-load performance of IPM machines considering both iron nonlinearity and rotor saliency.

This paper proposes a hybrid subdomain model which develops the improved boundary condition to predict the air-gap field of IPM machine under either open-circuit or on-load condition. The nonlinear boundary condition is derived from the modified MRN that represents the magnetic field of PMs, stator iron, and rotor iron. It is used to predict the air-gap field using subdomain technique. Compared with the conventional MRN, the air-gap reluctance is replaced by the subdomain model to improve the calculation speed and keep the MRN unchanged at different rotor position. In the proposed model, the field-network interface coupling connects the radial air flux and the tangential magnetic field strength of iron region, which is crucial for obtaining the on-load field of IPM machine. The modified MRN for the iron region can accurately show the influence of armature reaction on the rotor bridge of IPM machine, which is the key to represent the saliency effect. Iterative calculation is required to obtain the coupling value on the field-network interface using Newton-Raphson method. Hence, the proposed model can accurately describe the slotting effect, iron nonlinearity, and rotor saliency of IPM machines. Both FEM and experiment are carried out to validate HSM for flat-shaped and V-shaped IPM machines.

II. HYBRID SUBDOMAIN MODEL

The HSM is developed from the combination of subdomain technique and MRN to accurately predict on-load performance of IPM machine. In the constant permeability region, the subdomain technique is proposed to obtain the air-gap field with high computational efficiency and high accuracy while in the nonlinear permeability region, the modified magnetic reluctance network is employed to calculate the iron field in either regular
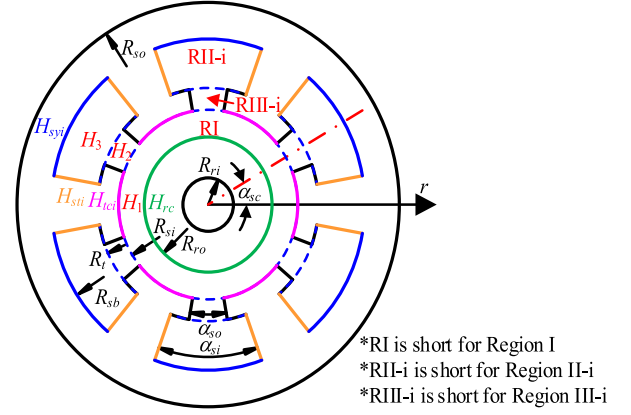

Fig. 1. The general subdomains for constant permeability region.

or irregular flux path. The interface coupling between the subdomain technique and the modified magnetic reluctance network is directly obtained according to the nonlinear boundary condition. Hence, the magnetic field distribution of IPM machine is predicted at any rotor position with any current excitation. Accordingly, its electromagnetic performance including flux linkage, back-EMF, and torque can be calculated.

A. Constant Permeability Region

The subdomain technique for constant permeability region requires the following assumptions: (1) The slot shape is simplified as shown in Fig. 1, but the influence of tooth-tip is considered; (2) The stator current is uniformly distributed in the slot region as well as the equivalent current representing the iron nonlinearity of tooth body and stator yoke; (3) The magnetic property of PMs is linear; (4) End effect is neglected.

In the three subdomains (Region I, Region II, and Region III), the general expression of analytical solution is given as:

$$A_{z1} = \sum_k \left\{ \left[A_1(r/R_{si})^k + B_1(r/R_{ro})^{-k} \right] \cos(k\alpha) \right.$$
$$\left. + \left[C_1(r/R_{si})^k + D_1(r/R_{ro})^{-k} \right] \sin(k\alpha) \right\} \quad (1)$$

$$A_{z2i} = \sum_n D_{2i} \left[G_2 \left(\frac{r}{R_{sb}} \right)^{E_n} + \left(\frac{r}{R_t} \right)^{-E_n} \right] \cdot$$
$$\cos \left[E_n \left(\alpha + \frac{\alpha_{si}}{2} - \alpha_i \right) \right] + \mu_0 J_{i0} \left(2R_{sb}^2 \ln r - r^2 \right) / 4 \quad (2)$$

$$A_{z3i} = \frac{\mu_0}{2} \frac{a_{si}}{\alpha_{so}} J_{i0} \left(R_{sb}^2 - R_t^2 \right) \ln r$$
$$+ \sum_m \left[C_{3i} \left(\frac{r}{R_t} \right)^{F_m} + D_{3i} \left(\frac{r}{R_{si}} \right)^{-F_m} \right]$$
$$\cos \left[F_m \left(\alpha + \frac{\alpha_{so}}{2} - \alpha_i \right) \right] \quad (3)$$

where A_{z1}, A_{z2i} and A_{z3i} are the vector potential in the air-gap, i^{th} slot-opening and i^{th} slot region ($i = 1,2,\ldots\ldots,Q_s$, where Q_s is the
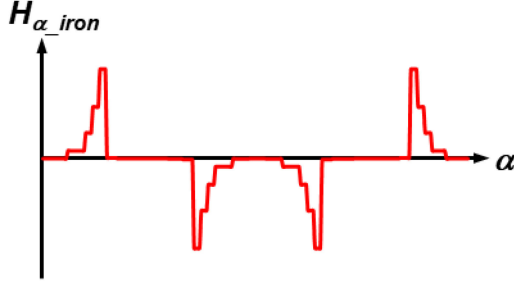
Fig. 2. The distribution of tangential field strength on either rotor outer surface (H_{rc}) or tooth-shoe surface (H_{sb}).

slot number) [25]. R_{ro}, R_{si}, R_t, and R_{sb} are the radii of rotor outer surface, stator bore, slot top, and slot bottom. α_{so}, α_{si}, and α_i are the angles for slot-opening, slot width and the central position of ith slot. Their definition can also be found in Fig. 1. J_{i0} is the equivalent current density in the ith slot region, representing the winding current and the nonlinearity of tooth-body and stator yoke. $E_n = n\pi/\alpha\_si$. $F_m = (m\pi)/\alpha_{so}$. $G_2 = (R_t/R_{sb})$. $A_1, B_1, C_1, D_1, D_{2i}, C_{3i}$, and D_{3i} will be derived from the modified boundary condition and interface between subdomains for IPM machines, which is discussed as follows.

1) Rotor Outer Surface: According to the electromagnetic theory [30], no surface current sheet can exist on the IPM rotor surface, and therefore the tangential field strength $H_{1\alpha}$ in the air-gap is equal to that in the iron H_{rc} at $r = R_r$:

$$H_{1\alpha}\,|_{r=R_{ro}} = -\frac{\partial A_{z1}}{\partial r} = H_{rc}(R_{ro}, \alpha) \quad (4)$$

H_{rc} is approximated as the step waveform, whose step length will influence both calculation time and accuracy, as shown in Fig. 2. Thus, H_{rc} can be directly expressed in the form of Fourier series and the following equation can be obtained from (4):

$$\begin{cases} k^2\,(A_1 G_1 - B_1) \\ = \sum_{j=1}^{N_{rotor}} \frac{2}{\pi}\mu_0 R_{ro} H_{rcj} \sin\left(\frac{k\alpha_{rotor}}{2}\right)\cos(k\alpha_j) \\ k^2\,(C_1 G_1 - D_1) \\ = \sum_{j=1}^{N_{rotor}} \frac{2}{\pi}\mu_0 R_{ro} H_{rcj} \sin\left(\frac{k\alpha_{rotor}}{2}\right)\sin(k\alpha_j) \end{cases} \quad (5)$$

where H_{rcj} is the tangential field strength of iron region on the rotor surface between $\alpha_j - \alpha_{rotor}/2$ and $\alpha_j + \alpha_{rotor}/2$. N_{rotor} is the number of divisions for rotor surface current. $G_1 = (R_{ro}/R_{si})$.

2) Stator Inner Bore: Based on the boundary condition of electromagnetic theory, the tangential field strength in the air-gap region are equal to that in the tooth-tip region, as show in Fig. 1:

$$\begin{cases} H_{1\alpha}\,|_{r=R_{si}} = H_{3\alpha}\,|_{r=R_{si}}, \alpha_i - \alpha_{so}/2 \le \alpha \le \alpha_i - \alpha_{so}/2 \\ H_{1\alpha}\,|_{r=R_{si}} = H_{sb}\,(r=R_{si}), \alpha < \alpha_i - \alpha_{so}/2\,\text{or}\,\alpha > \alpha_i - \alpha_{so}/2 \end{cases} \quad (6)$$

where H_{sb} is the tangential field strength in the tooth-tip. As shown in Fig. 2, the step wave is used to simplify the expression

of H_{sb}. Hence, the boundary condition can be manipulated as:

$$\begin{cases} k^2\,(A_1 - G_1 B_1) = \sum_{i=1}^{Q_s} \left\{ \frac{\mu_0 \alpha_{si}}{2\alpha_{so}} J_{i0}\left(R_{sb}^2 - R_t^2\right)\eta_{i0}+ \right. \\ \sum_m F_m\,(C_{3i}G_3 - D_{3i})\,\eta_i + \\ \left. \sum_{j=1}^{N_t} \frac{2\mu_0}{\pi} R_{si} H_{sbij} \sin\left(\frac{k\alpha_{tooth}}{2}\right)\cos(k\alpha_{ij}) \right\} \\ k^2\,(C_1 - G_1 D_1) = \sum_{i=1}^{Q_s} \left\{ \frac{\mu_0 \alpha_{si}}{2\alpha_{so}} J_{i0}\left(R_{sb}^2 - R_t^2\right)\xi_{i0}+ \right. \\ \sum_m F_m\,(C_{3i}G_3 - D_{3i})\,\xi_i + \\ \left. \sum_{j=1}^{N_t} \frac{2\mu_0}{\pi} R_{si} H_{sbij} \sin\left(\frac{k\alpha_{tooth}}{2}\right)\sin(k\alpha_{ij}) \right\} \end{cases} \quad (7)$$

where H_{sbij} is the tooth-shoe surface current between $\alpha_{ij} - \alpha_{tooth}/2$ and $\alpha_{ij} + \alpha_{tooth}/2$. N_{tooth} is the number of division for tooth surface current. $G_3 = (R_{so}/R_t)$. $\eta_{i0}, \eta_i, \xi_{i0}$, and ξ_i are given in Appendix.

Besides, as the vector potential is continuous on the interface between air-gap region and slot-opening region ($A_{z1}|_{r=R_s} = A_{z3}|_{r=R_s}$), the following equation can be obtained:

$$C_{3i}G_3 + D_{3i} = \sum_k \left[(A_1 + G_1 B_1)\sigma_i + (C_1 + G_1 D_1)\tau_i\right] \quad (8)$$

where σ_i and τ_i is defined in Appendix.

3) Interface Between Region II and III: On the interface of ith slot and i^{th} slot-opening, the equivalence of tangential field strength $H_{\alpha 2}$ and $H_{\alpha 3}$ at $r = R_t$ is used to deduce the following equation: [25]

$$\sum_m F_m\,(C_{3i} - D_{3i}G_3)\,\gamma = -E_n D_{2i}\left(G_2^2 - 1\right)$$

$$+ \frac{\mu_0 \alpha_{si}}{2\alpha_{so}} J_{i0}\left(R_{sb}^2 - R_t^2\right)\gamma_0 \quad (9)$$

where γ and γ_0 are given in Appendix. Besides, due to the continuation of A_{z2} and A_{z3} at $r = R_t$, it can be calculated that

$$C_{3i} + D_{3i}G_3 = \sum_n D_{2i}\left(G_2^2 + 1\right)\zeta \quad (10)$$

where ζ is defined in Appendix [25]. According to (1)-(10), the magnetic field distribution in the constant permeability region can be directly calculated. However, the equivalent current density on the ith slot J_{i0}, the tangential field strength on the rotor outer surface H_{rc} and on the tooth-shoe surface H_{sb} should be obtained first.

B. Nonlinear Permeability Region

The aims of calculating the magnetic field in the nonlinear permeability region are to obtain the value of H_{rc}, H_{sb}, and J_{i0} and therefore quantifies the influence of iron nonlinearity on the machine performance. Since the iron permeability is nonlinear, only magnetic-circuit-based model can precisely calculate its field distribution besides FEM. In this paper, the MRN is used to predict the iron near the air-gap region. No prior knowledge is required to establish the reluctance network as it will follow the rectangular or fan-shaped mesh principle to calculate the reluctance. Fig. 3 gives generalized reluctance network in HSM, which is suitable for both flat-shaped and V-shaped IPM machines. The mesh sizes of surface iron (e.g., tooth-shoe and
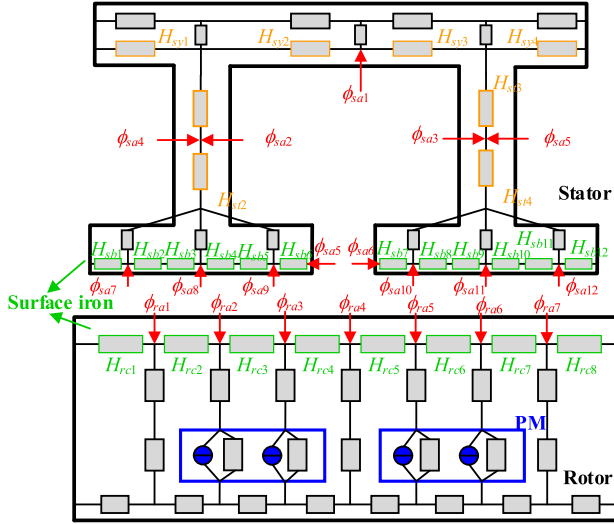
Fig. 3. The modified magnetic reluctance network for IPM machine.

Fig. 4. The solving process of hybrid subdomain model for IPM machine at t_0.

rotor surface) are small to accurately represent the tangential field strength for both machines. The shape of rotor pole shoe is approximated as trapezoidal while the rotor bridge is regarded as annular sector for both machines. The magnetic reluctance in the rotor yoke, stator yoke, and stator tooth body are calculated using the roughly divided iron as their fluxes are uniformly distributed. Both IPM machines share the same topology of MRN of Fig. 3 and their main differences are the different geometry of iron region to obtain the value of magnetic reluctance.

The calculation of iron reluctance is derived from the geometry of the rectangular or fan-shaped mesh. The radial reluctance and tangential reluctance for fan-shaped reluctance and the rectangular reluctance are expressed as:

$$\begin{cases} R_{radial} = \ln(r_2/r_1)/(\mu_r \alpha_m l_{ef}) \\ R_{tangential} = \alpha_m/\mu_r l_{ef} \ln(r_2/r_1) \\ R_{rectangular} = w_{rect}/\mu_r a_{rect} l_{ef} \end{cases} \quad (11)$$

where r_1 and r_2 are the radii of the inner and outer surface for the fan-shaped iron region and α_m is the angle of the fan-shaped iron region. w_{rect} and a_{rect} are the width and length of the rectangular iron region. u_r is the iron permeability and l_{ef} is the effective length of IPM machine [10]–[16]. The magnetic voltage for PM is calculated by:

$$F_m = H_c * h_m \quad (12)$$

where H_c is the coercivity of PM and h_m is the magnet thickness in the magnetization direction.

C. Field-Network Interface Coupling

In HSM, the air-gap field is obtained using subdomain technique while the magnetic voltage distribution of iron region is calculated from the magnetic reluctance network. For the boundary condition on the rotor outer surface and stator bore, the tangential field strength is approximated as step wave according to the mesh size of iron region. Hence, the number of magnetic
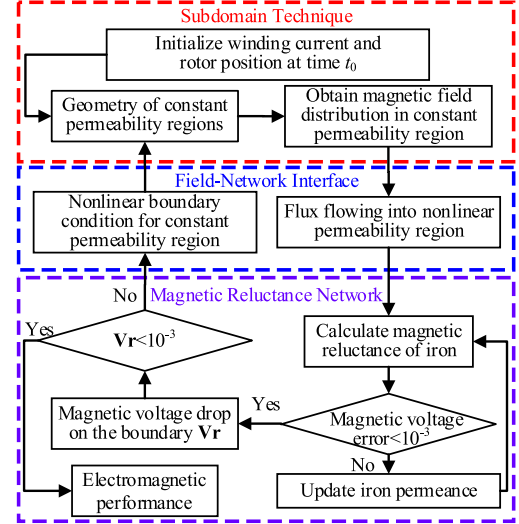
reluctances on these boundaries are much larger than the rotor yoke and stator yoke. As for J_{i0}, both winding current and the magnetic voltage drop of the iron region around the slot are regarded as the uniformly distributed current in the slot region. It can be calculated as:

$$J_{i0} = \frac{Q_s(R_{sb} - R_t)(H_{sti} - H_{st(i-1)}) + \pi(R_{sb} + R_{so})H_{syi}}{Q_s A_{slot}} \quad (13)$$

where H_{sti} and H_{syi} are the magnetic field strength of the ith tooth-body and stator yoke. R_{so} is stator outer radius and A_{slot} is the slot area Such simplification has negligible influence on the air-gap field distribution. Hence, it can be seen that the tangential field strength of iron region is the key to obtain the analytical solution of air-gap field using the subdomain technique.

As for the flux from air-gap, slot-opening and slot region, it can be derived from the vector potential in the subdomain model:

$$\phi_a = l_{ef} [A_z(r_1, \alpha_1) - A_z(r_2, \alpha_2)] \quad (14)$$

where $A_z(r_1, \alpha_1)$ and $A_z(r_2, \alpha_2)$ are the vector potential at the initial position and final position for integral. Hence, the calculation loop is established between the MRN and the subdomain model. According to the Kirchhoff's law, the HSM in Fig. 3 can be solved using Newton-Raphson method, where the flux from slot and air-gap is represented by the function of magnetic potential in the iron. Fig. 4 shows the solving process for obtaining the electromagnetic performance of IPM machine at time t_0.

It is noted that the same MRN is used at different rotor position under either open-circuit condition or on-load condition. The air reluctance is replaced by the subdomain model in HSM and therefore the corresponding flux flowing into the stator and rotor can be analytically obtained with the unchanged MRN. Considerable reluctance representing rotor surface iron is used to obtain the accurate tangential field strength on the boundary and account for the rotor saliency. Hence, the rotor bridge saturation
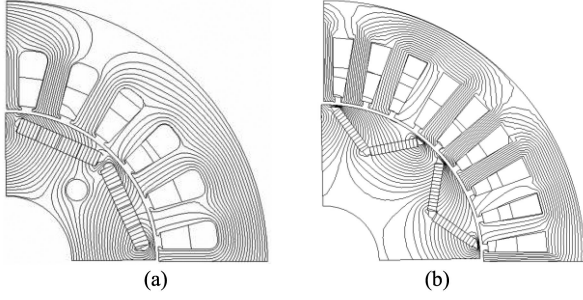
Fig. 5. The flux distribution of IPM machines at rated load: (a) flat-shaped rotor and (b) V-shaped rotor.

TABLE I
THE PARAMETERS OF FLAT-SHAPED AND V-SHAPED IPM MACHINES

Parameter	Flat-shaped rotor	V-shaped rotor
Pole number	4	8
Slot number	24	36
Coil pitch	5	4
Remanence	1.10T	1.22T
Stator outer diameter	120 mm	245mm
Rated current amplitude	40A	200A
Rated speed	15000rpm	2800rpm
Rated power	11kW	47kW

due to PM and armature reaction can be precisely exhibited from the rotor surface reluctance in the HSM. The proposed model is valid for IPM machines at different saliency control angle.

Hence, the phase flux linkage can be calculated from the air-gap field flux density:

$$\psi_{Phase} = N_c l_{ef} \sum_i [A_{z1}(R_s, \alpha_i) - A_{z1}(R_s, \alpha_{i+\tau})] \quad (15)$$

where N_c is coil conductors for one phase and τ is the coil pitch. Therefore, α_i and $\alpha_{i+\tau}$ represent the coil position belonging to the same phase. The phase back-EMF is calculated by the derivative of phase flux linkage to time:

$$E_{Phase} = \frac{d\psi_{Phase}}{dt} \quad (16)$$

The electromagnetic torque is derived from the integral of Maxwell tensor along the middle path of air-gap region:

$$T_e = -\frac{l_{ef}r}{\mu_0} \int_0^{2\pi} \frac{\partial A_{z1}(r, \alpha)}{\partial \alpha} \frac{\partial A_{z1}(r, \alpha)}{\partial r} d\alpha \quad (17)$$

III. FE AND EXPERIMENT VALIDATION

Two IPM machines are built to validate the proposed HSM and analytically compare their performances. They have double-layer short-pitch windings with star connection. The coil pitch is 5 and 4 for flat-shaped and V-shaped IPM machines, respectively. The HSMs for both IPM machines are calculated on MATLAB while their flux distributions are obtained from JMAG, Fig. 5. Their main parameters are shown in Table I. The test rig for both IPM machines are given in Fig. 6
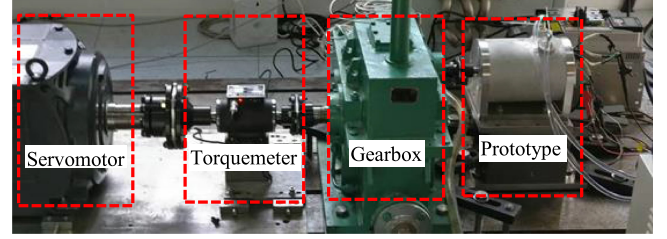

Fig. 6. The test rig for both IPM machines with inverter.
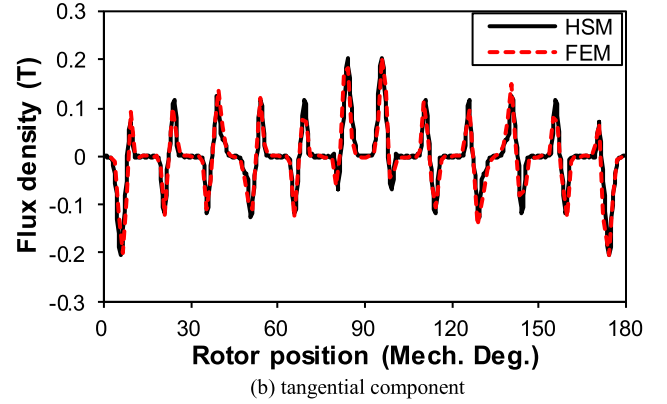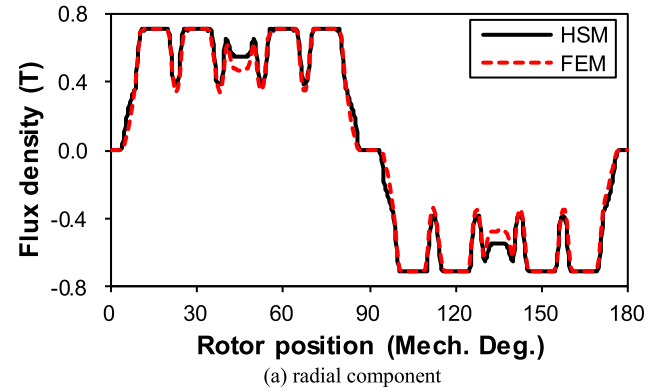

Fig. 7. The open-circuit air-gap flux density for flat-shaped IPM machine when the rotor bridge is near the slot-opening (a) radial component, (b) tangential component.

The air-gap field calculated by HSM for both IPM machines are compared with FEM results, as shown in Figs. 7–10. Both radial and tangential component of flux density using HSM under either open-circuit condition or on-load condition are close to those using FEM. Hence, the flux linkage, back-EMF, and torque can be obtained according to the air-gap field distribution, and the experimental back-EMF validate the high accuracy of HSM, as shown in Figs. 11–14. Comparing with the experiment result, the errors of back-EMF amplitude using HSM is 2.5% and 4.7% for flat-shaped and V-shaped IPM machines, respectively. Figs. 15, 16 compare the cogging torque using HSM and FEM. HSM predictions agree well with FEM results for both IPM machines. Figs. 17–18 show that the torque waveforms predicted using HSM are slightly smaller than FEM results due to the modelling simplification of MRN. The average errors of HSM
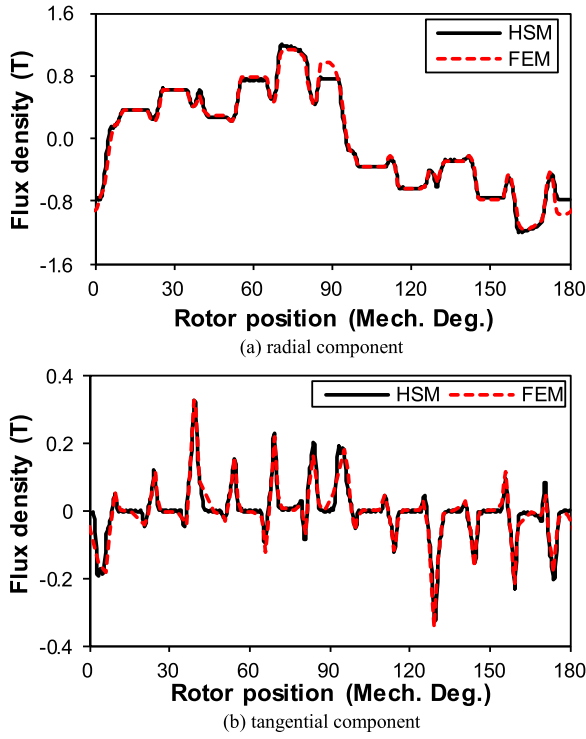
Fig. 8. The open-load air-gap flux density for flat-shaped IPM machine when the rotor bridge is near the slot-opening $I_m = 40A$ (a) radial component, (b) tangential component.
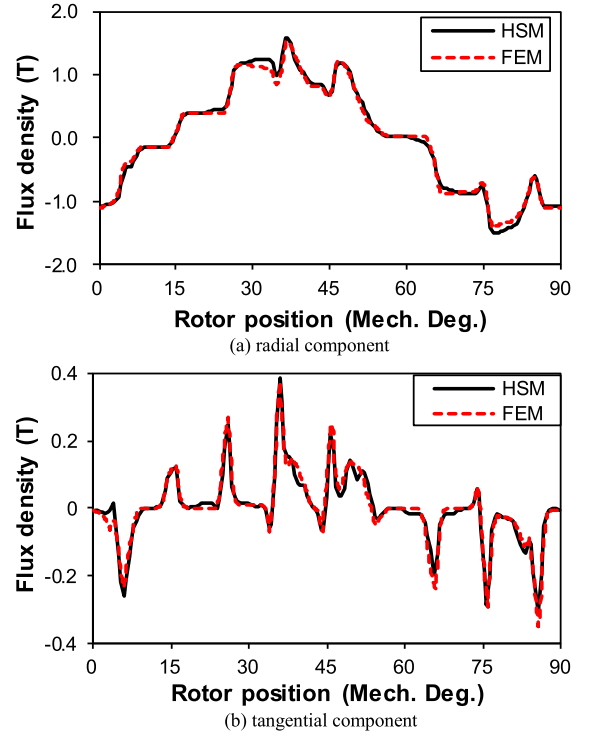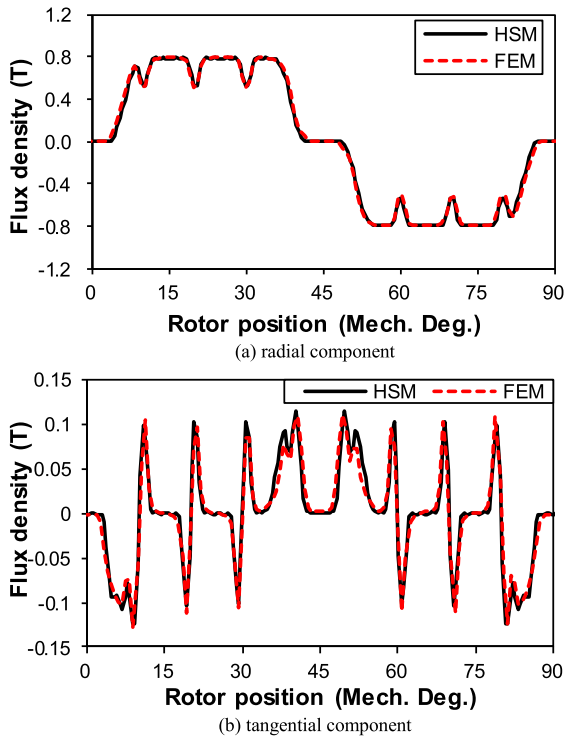

Fig. 9. The open-circuit air-gap flux density for V-shaped IPM machine when the rotor bridge is near the slot-opening (a) radial component, (b) tangential component.

Fig. 10. The open-load air-gap flux density for V-shaped IPM machine when the rotor bridge is near the slot-opening $I_m = 200A$ (a) radial component, (b) tangential component.
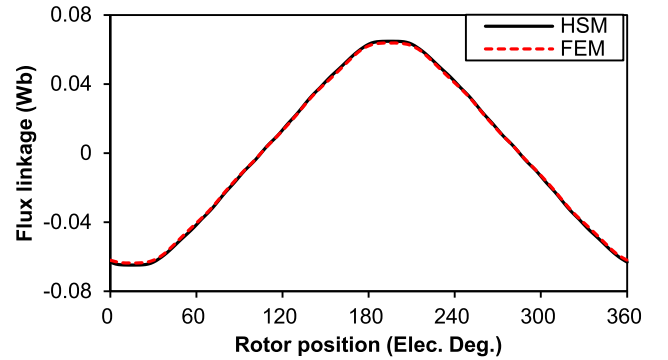

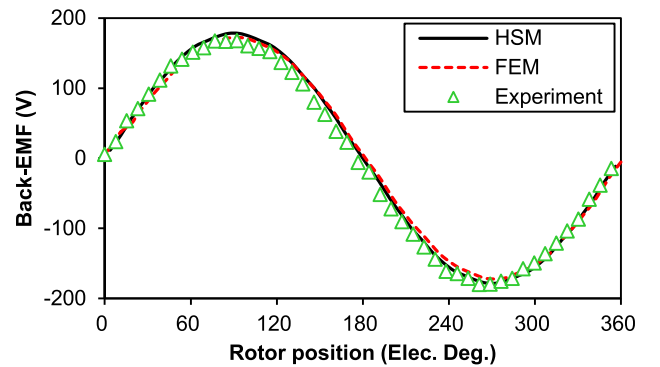Fig. 11. The phase flux linkage waveform of flat-shaped IPM machine under open-circuit condition.

Fig. 12. The line-to-line back-EMF waveform of flat-shaped IPM machine under open-circuit condition.

Fig. 13. The phase flux linkage waveform of V-shaped IPM machine under open-circuit condition.

Fig. 14. The line-to-line back-EMF waveform of V-shaped IPM machine under open-circuit condition.
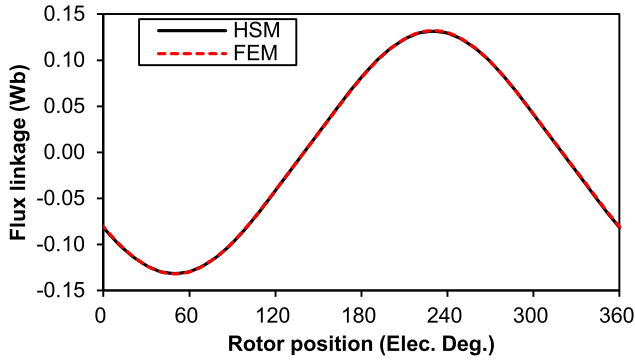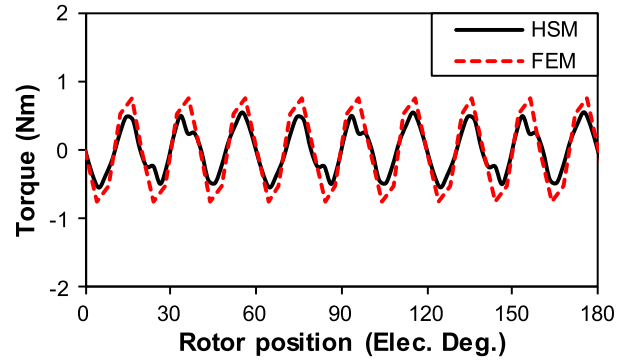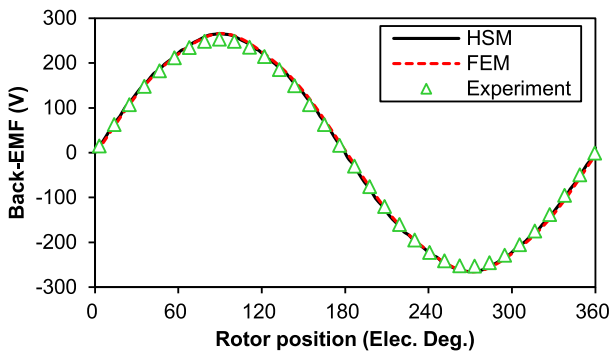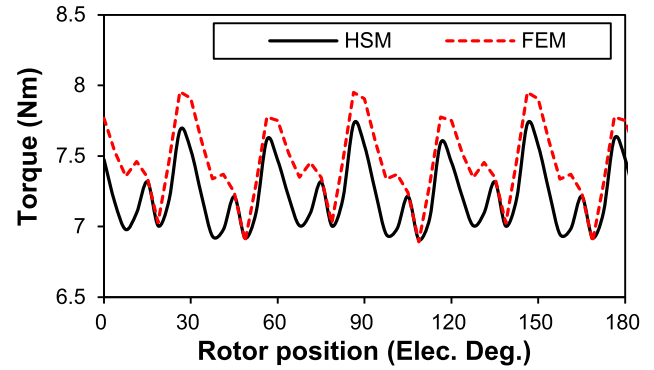

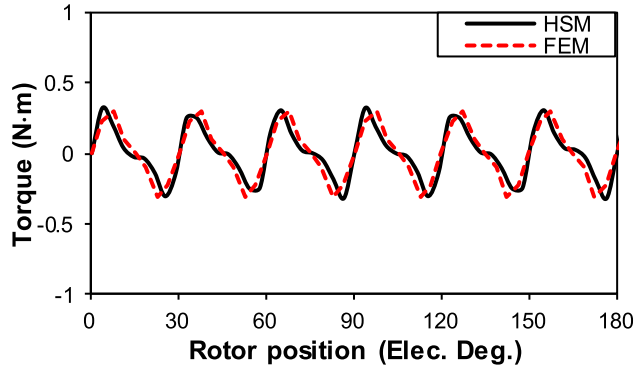Fig. 15. The cogging torque waveform of flat-shaped IPM machine.

Fig. 16. The cogging torque waveform of V-shaped IPM machine.

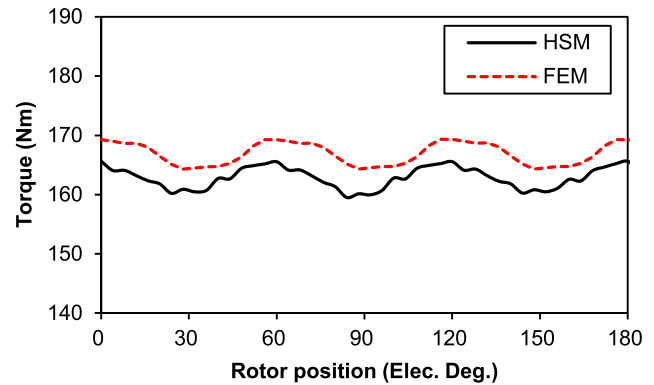Fig. 17. The torque waveform of flat-shaped IPM machine at $I_m = 40$A.

Fig. 18. The torque waveform of V-shaped IPM machine at $I_m = 200$A.

predictions are 3.1% and 2.4% for flat-shaped and V-shaped IPM machines, which exhibits the high accuracy of HSM.

In the IPM machines, the reluctance torque will contribute to the average torque and therefore the maximum torque per ampere (MTPA) control method is usually employed. The angle between the current component aligned with q-axis and the total stator current is defined as saliency control angle. It represents the saliency level of IPM machines, Figs. 17, 18. The IPM machines will output the maximum toque when their saliency control angles are 14° and 32° for flat-shaped and V-shaped

IPM machines at rated current, respectively. It shows that the V-shaped IPM machines has larger reluctance torque than flat-shaped IPM machines due to flux-focusing effect. Besides, HSM can accurately predict the average torque at different saliency control angle, whose average errors are 2.3% and 4.5%, respectively.

Hence, the saliency control angle for the maximum output torque can be obtained at different current amplitude. The torque comparison between HSM and FEM for flat-shaped IPM machines is given in Fig. 21. The average torque using HSM is close to FEM calculation and experimental results, whose average
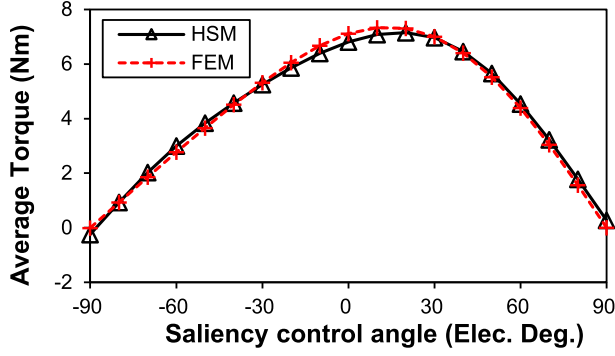
Fig. 19.   The relationship between the average torque and saliency control angle for flat-shaped IPM machine at $I_m = 40$A.
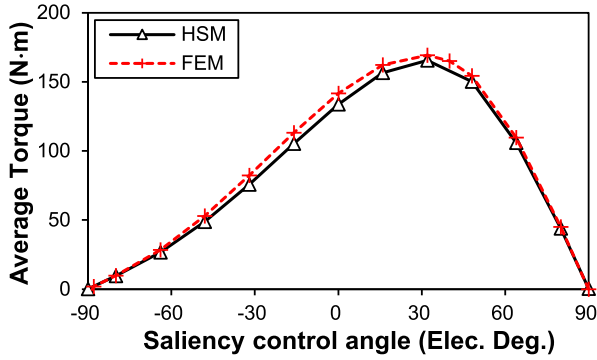

Fig. 20.   The relationship between the average torque and saliency control angle for V-shaped IPM machine at $I_m = 200$A.
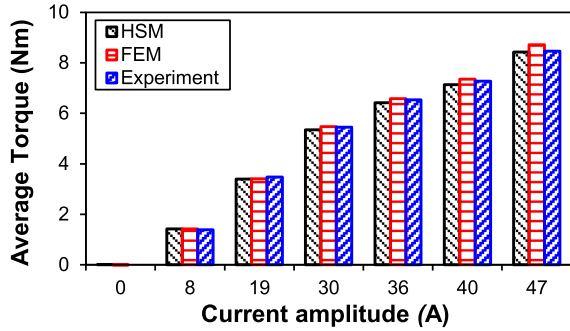

Fig. 21.   The relationship between the average torque and current amplitude using MTPA control for flat-shaped IPM machine.
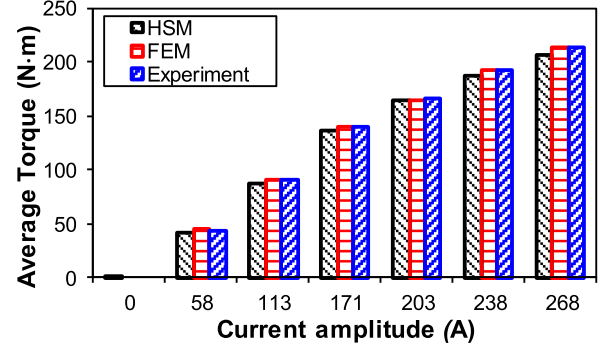

Fig. 22.   The relationship between the average torque and current amplitude at saliency control angle 20° for V-shaped IPM machine.

TABLE II
CALCULATION TIME OF HSM AND FEM FOR BOTH MACHINES

Saliency control angle (Elec. Deg.)		-90	-45	0	45	90
Flat-shape IPM machine	HSM (s)	57	64	56	54	68
	FEM (s)	310	326	307	304	294
V-shape IPM machine	HSM (s)	51	57	74	71	66
	FEM (s)	440	407	322	343	400

IV. CONCLUSION

This paper introduces a hybrid subdomain model for predicting the flat-shaped and V-shaped IPM machines considering slotting effect, iron nonlinearity and rotor saliency. As far as the authors know, it's the first time that the subdomain technique is employed to predict the on-load performance of these two kinds of IPM machines considering saliency effect. The MRN is modified to incorporate the subdomain technique based on the theory of field-network interface coupling and therefore it will increase the computational efficiency. Besides, the proposed model can accurately account for the reluctance torque at different saliency control angle, which makes it powerful to obtain the electromagnetic performance of IPM machines using MTPA control strategy. Both FEM and experiment demonstrate the high accuracy and low computational burden of the proposed model.

APPENDIX

η_{i0}, η_i, ξ_{i0}, ξ_i, σ_i, and τ_i represent the Fourier series transformation between the slot-opening and air-gap. Their expressions are given as follows:

$$\eta_i(m, k) = -\frac{1}{\pi} \frac{k^2}{F_m^2 - k^2} [\cos(m\pi)\sin(k\alpha_i + k\alpha_{so}/2)$$
$$- \sin(k\alpha_i - k\alpha_{so}/2)] \tag{18}$$

$$\xi_i(m, k) = \frac{1}{\pi} \frac{k^2}{F_m^2 - k^2} \cdot [\cos(m\pi)\cos(k\alpha_i + k\alpha_{so}/2)$$
$$- \cos(k\alpha_i - k\alpha_{so}/2)] \tag{19}$$

$$\eta_{i0}(k) = \frac{2}{\pi} \sin(k\alpha_{so}/2)\cos(k\alpha_i) \tag{20}$$

error is 2.0%. In Fig. 22, the V-shape IPM machine is operated at constant saliency control angle and the average error of HSM predictions is 2.6%. The measured current amplitude is 203A at rated load and the torque error is 0.5%. The measured current amplitude is 203A at rated load and the torque error is 0.5% for V-shaped IPM machine.

The computational time between HSM and FEM is given in Table II. The HSM can save more than 77% computational resource of FEM and therefore accelerate the process of initial design and optimization for IPM machines.

$$\xi_{i0}(k) = \frac{2}{\pi} \sin{(k\alpha_{so}/2)} \sin{(k\alpha_i)} \tag{21}$$

$$\sigma_i(m,k) = \frac{2\pi}{k\alpha_{si}} \eta_i(m,k) \tag{22}$$

$$\tau_i(m,k) = \frac{2\pi}{k\alpha_{si}} \xi_i(m,k) \tag{23}$$

As for the Fourier series transformation between the slot and slot-opening, γ_0, γ, and ζ are given as: [25]

$$\gamma_0(n) = \frac{4}{n\pi} \cos{\left(\frac{n\pi}{2}\right)} \sin{\left(\frac{E_n \alpha_{so}}{2}\right)} \tag{24}$$

$$\gamma(m,n) = -\frac{2}{\alpha_{si}} \frac{E_n}{F_m^2 - E_n^2} \cdot \left[\cos(m\pi) \sin{\left(E_n \frac{\alpha_{si} + \alpha_{so}}{2}\right)} \right.$$
$$\left. - \sin{\left(E_n \frac{\alpha_{si} - \alpha_{so}}{2}\right)} \right] \tag{25}$$

$$\zeta(m,n) = \frac{\alpha_{si}}{\alpha_{so}} \gamma(m,n) \tag{26}$$

REFERENCES

[1] K. T. Chau, C. C. Chan, and C. Liu, "Overview of permanent-magnet brushless drives for electric and hybrid electric vehicles," *IEEE Trans. Ind. Electron.*, vol. 55, no. 6, pp. 2246–2257, Jun. 2008.

[2] N. Bianchi, S. Bolognani, M. Zigliotto, and M. Zordan, "Innovative remedial strategies for inverter faults in IPM synchronous motor drives," *IEEE Trans. Energy Conver.*, vol. 18, no. 2, pp. 306–314, Jun. 2003.

[3] H. Seol, J. Lim, D. Kang, J. S. Park, and J. Lee, "Optimal design strategy for improved operation of IPM BLDC motors with low-resolution hall sensors," *IEEE Trans. Ind. Electron.*, vol. 64, no. 12, pp. 9758–9766, Dec. 2017.

[4] G. Kang, Y. Son, G. Kim, and J. Hur, "A novel cogging torque reduction method for interior-type permanent-magnet motor," *IEEE Trans. Ind. Appl.*, vol. 45, no. 1, pp. 161–167, Jan. 2009.

[5] T. Ohnishi and N. Takahashi, "Optimal design of efficient IPM motor using finite element method," *IEEE Trans. Magn.*, vol. 36, no. 5, pp. 3537–3539, Sep. 2000.

[6] J. Lee and B. Kwon, "Optimal rotor shape design of a concentrated flux IPM-type motor for improving efficiency and operation range," *IEEE Trans. Magn.*, vol. 49, no. 5, pp. 2205–2208, May 2013.

[7] K. Nakamura, K. Saito, and O. Ichinokura, "Dynamic analysis of interior permanent magnet motor based on a magnetic circuit model," *IEEE Trans. Magn.*, vol. 39, no. 5, pp. 3250–3252, Sep. 2003.

[8] C. Mi, M. Filippa, W. Liu, and R. Ma, "Analytical method for predicting the air-gap flux of interior-type permanent-magnet machines," *IEEE Trans. Magn.*, vol. 40, no. 1, pp. 50–58, Jan. 2004.

[9] L. Zhu, S. Z. Jiang, Z. Q. Zhu, and C. C. Chan, "Analytical modeling of open-circuit air-gap field distributions in multisegment and multilayer interior permanent-magnet machines," *IEEE Trans. Magn.*, vol. 45, no. 8, pp. 3121–3130, Aug. 2009.

[10] X. Huang, M. Zhu, W. Chen, J. Zhang, and Y. Fang, "Dynamic reluctance mesh modeling and losses evaluation of permanent magnet traction motor," *IEEE Trans. Magn.*, vol. 53, no. 6, pp. 1–4, Jun. 2017.

[11] N. Elloumi, M. Bortolozzi, A. Masmoudi, M. Mezzarobba, M. Olivo, and A. Tessarolo, "Numerical and analytical approaches to the modeling of a spoke type ipm machine with enhanced flux weakening capability," *IEEE Trans. Ind. Appl.*, vol. 55, no. 5, pp. 4702–4714, Sep. 2019.

[12] K. D. Hoang, "Simplified analytical model for rapid evaluation of interior pm traction machines considering magnetic nonlinearity," *IEEE Open J. Ind. Electron. Soc.*, vol. 1, pp. 340–354, 2020.

[13] J. W. Kwon, M. Li, and B. I. Kwon, "Design of V-type consequent-pole IPM machine for pm cost reduction with analytical method," *IEEE Access*, vol. 9, pp. 77386–77397, 2021.

[14] G. Liu, S. Jiang, W. Zhao, and Q. Chen, "Modular reluctance network simulation of a linear permanent-magnet vernier machine using new mesh generation methods," *IEEE Trans. Ind. Electron.*, vol. 64, no. 7, pp. 5323–5332, Jul. 2017.

[15] D. Cao, W. Zhao, J. Ji, and Y. Wang, "Parametric equivalent magnetic network modeling approach for multi-objective optimization of PM machine," *IEEE Trans. Ind. Electron.*, vol. 68, no. 8, pp. 6619–6629, Aug. 2021.

[16] G. Liu, Y. Wang, Q. Chen, G. Xu, and D. Cao, "Design and analysis of a new equivalent magnetic network model for IPM machines," *IEEE Trans. Magn.*, vol. 56, no. 6, pp. 1–12, Jun. 2020.

[17] L. Ding, G. Liu, Q. Chen, and G. Xu, "A novel mesh-based equivalent magnetic network for performance analysis and optimal design of permanent magnet machines," *IEEE Trans. Energy Convers.*, vol. 34, no. 3, pp. 1337–1346, Sep. 2019.

[18] D. Cao, W. Zhao, J. Ji, L. Ding, and J. Zheng, "A generalized equivalent magnetic network modeling method for vehicular dual-permanent-magnet vernier machines," *IEEE Trans. Energy Convers.*, vol. 34, no. 4, pp. 1950–1962, Dec. 2019.

[19] A. Balamurali, C. Lai, A. Mollaeian, V. Loukanov, and N. C. Kar, "Analytical investigation into magnet eddy current losses in interior permanent magnet motor using modified winding function theory accounting for pulsewidth modulation harmonics," *IEEE Trans. Magn.*, vol. 52, no. 7, pp. 1–5, Jul. 2016.

[20] P. Liang, Y. Pei, F. Chai, Y. Bi, and S. Cheng, "An improved method for armature-reaction magnetic field calculation of interior permanent magnet motors," *IEEE Trans. Magn.*, vol. 52, no. 7, pp. 1–4, Jul. 2016.

[21] Q. Li, T. Fan, and X. Wen, "Armature-reaction magnetic field analysis for interior permanent magnet motor based on winding function theory," *IEEE Trans. Magn.*, vol. 49, no. 3, pp. 1193–1201, Mar. 2013.

[22] M. Farshadnia, M. A. M. Cheema, R. Dutta, and J. E. Fletcher, "Analytical modeling of armature reaction air-gap flux density considering the non-homogeneously saturated rotor in a fractional-slot concentrated-wound IPM machine," *IEEE Trans. Magn.*, vol. 53, no. 2, pp. 1–12, Feb. 2017.

[23] P. Akiki *et al.*, "Nonlinear analytical model for a multi-V-shape ipm with concentrated winding," *IEEE Trans. Ind. Appl.*, vol. 54, no. 3, pp. 2165–2174, May 2018.

[24] Z. Q. Zhu, L. J. Wu, and Z. P. Xia, "An accurate subdomain model for magnetic field computation in slotted surface-mounted permanent-magnet machines," *IEEE Trans. Magn.*, vol. 46, no. 4, pp. 1100–1115, Apr. 2010.

[25] L. J. Wu, Z. Q. Zhu, D. Staton, M. Popescu, and D. Hawkins, "Subdomain model for predicting armature reaction field of surface-mounted permanent-magnet machines accounting for tooth-tips," *IEEE Trans. Magn.*, vol. 47, no. 4, pp. 812–822, Apr. 2011.

[26] L. J. Wu, Z. Q. Zhu, D. A. Staton, M. Popescu, and D. Hawkins, "Comparison of analytical models of cogging torque in surface-mounted PM machines," *IEEE Trans. Ind. Electron.*, vol. 59, no. 6, pp. 2414–2425, Jun. 2012.

[27] Tim C. O'Connell and P.T. Krein, "A Schwarz-Christoffel-based analytical method for electric machine field analysis," *IEEE Trans. Energy Convers.*, vol. 24, no. 3, pp. 565–577, Sep. 2009.

[28] D. Zarko, D. Ban, and T. A. Lipo, "Analytical calculation of magnetic field distribution in the slotted air gap of a surface permanent-magnet motor using complex relative air-gap permeance," *IEEE Trans. Magn.*, vol. 42, no. 7, pp. 1828–1837, Jul. 2006.

[29] L. J. Wu, Z. Li, X. Huang, Y. Zhong, Y. Fang, and Z. Q. Zhu, "A hybrid field model for open-circuit field prediction in surface-mounted PM machines considering saturation," *IEEE Trans. Magn.*, vol. 54, no. 6, pp. 1–12, Jun. 2018.

[30] L. J. Wu, Z. Li, D. Wang, H. Yin, X. Huang, and Z. Q. Zhu, "On-load field prediction of surface-mounted PM machines considering nonlinearity based on hybrid field model," *IEEE Trans. Magn.*, vol. 55, no. 3, pp. 1–11, Mar. 2019.

[31] L. Wu, H. Yin, D. Wang, and Y. Fang, "A nonlinear subdomain and magnetic circuit hybrid model for open-circuit field prediction in surface-mounted PM machines," *IEEE Trans. Energy Convers.*, vol. 34, no. 3, pp. 1485–1495, Sep. 2019.

[32] L. Wu, H. Yin, D. Wang, and Y. Fang, "On-load field prediction in SPM machines by a subdomain and magnetic circuit hybrid model," *IEEE Trans. Ind. Electron.*, vol. 67, no. 9, pp. 7190–7201, Sep. 2020.

[33] M.S. Mirazimi and A. Kiyoumarsi, "Magnetic field analysis of multi-flux-barrier interior permanent-magnet motors through conformal mapping," *IEEE Trans. Magn.*, vol. 53, no. 12, pp. 1–12, Dec. 2017.

[34] Z. Li, X. Huang, L. Wu, T. Long, B. Shi, and H. Zhang, "Open-circuit field prediction of interior permanent-magnet motor using hybrid field model accounting for saturation," *IEEE Trans. Magn.*, vol. 55, no. 7, Jul. 2019, Art. no. 8104707.

[35] Z. Zhang, C. Xia, Y. Yan, Q. Geng, and T. Shi, "A hybrid analytical model for open-circuit field calculation of multilayer interior permanent magnet machines," *J. Magn. Magn. Mater.*, vol. 435, pp. 136–145, 2017.

[36] D. Lim, K. Yi, D. Woo, H. Yeo, J. Ro, C. Lee, and H. Jung, "Analysis and design of a multi-layered and multi-segmented interior permanent magnet motor by using an analytic method," *IEEE Trans. Magn.,* vol. 50, no. 6, pp. 1–8, 2014.

[37] P. Liang, F. Chai, L. Chen, and Y. Wang, "Analytical prediction of no-load stator iron losses in spoke-type permanent-magnet synchronous machines," *IEEE Trans. Energy Convers.,* vol. 33, no. 1, pp. 252–259, Mar. 2018.

[38] M. Hajdinjak and D. Miljavec, "Analytical calculation of the magnetic field distribution in slotless brushless machines with U-shaped interior permanent magnets," *IEEE Trans. Ind. Electron.,* vol. 67, no. 8, pp. 6721–6731, Aug. 2020.

[39] Z.K. Li, X.Y. Huang, L.J. Wu, H. Zhang, T.N. Shi, Y. Yan, B Shi, and G. Yang,, "An improved hybrid field model for calculating on-load performance of interior permanent-magnet motors," *IEEE Trans. Ind. Electron.,* vol. 68, no. 10, pp. 9207–9217, Oct. 2021.

[40] P. Liang, F. Chai, Y. Li, and Y. Pei, "Analytical prediction of magnetic field distribution in spoke-type permanent-magnet synchronous machines accounting for bridge saturation and magnet shape," *IEEE Trans. Ind. Electron.,* vol. 64, no. 5, pp. 3479–3488, May 2017.

[41] P. Liang, F. Chai, Y. Yu, and L. Chen, "Analytical model of a spoke-type permanent magnet synchronous in-wheel motor with trapezoid magnet accounting for tooth saturation," *IEEE Trans. Ind. Electron.*, vol. 66, no. 2, pp. 1162–1171, Feb. 2019.

[42] M. Pourahmadi-Nakhli, A. Rahideh, and M. Mardaneh, "Analytical 2-D model of slotted brushless machines with cubic spoke-type permanent magnets," *IEEE Trans. Energy Conver.*, vol. 33, no. 1, pp. 373–382, Mar. 2018.

[43] L. Roubache, K. Boughrara, F. Dubas, and R. Ibtiouen, "New subdomain technique for electromagnetic performances calculation in radial-flux electrical machines considering finite soft-magnetic material permeability," *IEEE Trans. Magn.*, vol. 54, no. 4, pp. 1–15, Apr. 2018.

[44] Y. Zhou and Z.Q. Xue, "Analytical method for calculating the magnetic field of spoke-type permanent-magnet machines accounting for eccentric magnetic pole," *IEEE Trans. Ind. Electron.*, vol. 68, no. 3, pp. 2096–2107, Mar. 2021.

[45] B. Guo, Y. Huang, F. Peng, and J. Dong, "A new hybrid method for magnetic field calculation in IPMSM accounting for any rotor configuration," *IEEE Trans. Ind. Electron.,* vol. 66, no. 7, pp. 5015–5024, Jul. 2019.

Zhuo Chen was born in Sichuan Province, China, in 1996. He received the B.S. degree in 2018 in electrical engineering from Zhejiang University, Hangzhou, China, where he is currently working toward the Ph.D. degree in electrical machines and drives. His current research interests include the design of permanent-magnet machines for aerospace and traction applications.

Lijian Wu (Senior Member, IEEE) received the B.Eng. and M.Sc. degrees in electrical engineering from the Hefei University of Technology, Hefei, China, in 2001 and 2004, respectively, and the Ph.D. degree in electrical engineering from the University of Sheffield, Sheffield, U.K., in 2011. From 2004 to 2007, he was an Engineer with Delta Electronics (Shanghai) Company, Ltd. From 2012 to 2013, he was with Sheffield Siemens Wind Power Research Center, as a Design Engineer focusing on wind power generators. From 2013 to 2016, he was an Advanced Engineer with Siemens Wind Power A/S, Denmark. Since 2016, he has been with Zhejiang University, where he is currently a Professor of electrical machines and control systems. His current main research interests include design and control of permanent magnet machines.

Yiming Shen was born in Hangzhou, China, in 1993. He received the B.Eng. and Ph.D. degrees in electrical engineering from Zhejiang University, Hangzhou, China, in 2015 and 2020, respectively. He is currently a Postdoctoral Researcher with the College of Electrical Engineering, Zhejiang University. His research interests include design and analysis of novel permanent magnet machines with particular reference to linear machines for direct drive applications.

Zhaokai Li was born in Lishui, China, in 1993. He received the B.S. and Ph.D. degrees in electrical engineering from Zhejiang University, Hangzhou, China, in 2015 and 2020, respectively. He is currently a Postdoctoral Researcher with Zhejiang University. His main research interests include the analytical modeling of PMSM and iron loss analysis.

Tingna Shi (Member, IEEE) was born in Yuyao, China, in 1969. She received the B.S. and M.S. degrees in electrical engineering from Zhejiang University, Hangzhou, China, in 1991 and 1996, respectively, and the Ph.D. degree in electrical engineering from Tianjin University, Tianjin, China, in 2009. She is currently a Professor with the College of Electrical Engineering, Zhejiang University. Her current research interests include electrical machines and their control systems, power electronics, and electric drives.

Xiaoyan Huang (Member, IEEE) received the B.E. degree in control measurement techniques and instrumentation from Zhejiang University, Hangzhou, China, in 2003 and the Ph.D. degree in electrical machines and drives from the University of Nottingham, Nottingham, U.K., in 2008. From 2008 to 2009, she was a Research Fellow with the University of Nottingham. She is currently a Professor with the College of Electrical Engineering, Zhejiang University, where she is working on electrical machines and drives. Her research interests include PM machines and drives for aerospace and traction applications, and generator system for urban networks.